Design of binary Nb2O5–SiO2 self-standing monoliths bearing hierarchical porosity and their efficient Friedel–Crafts alkylation/acylation catalytic properties

Isabelle Ly, Elodie Layan, Emmanuel Picheau, Nicolas Chanut, Frédéric Nallet, Ahmed Bentaleb, Marie-Anne Dourges, Roland Pellenq, Elizabeth Hillard, Thierry Toupance, et al.

Design of Binary Nb_2O_5–SiO_2 Self-Standing Monoliths Bearing Hierarchical Porosity and Their Efficient Friedel–Crafts Alkylation/Acylation Catalytic Properties

Isabelle Ly, Elodie Layan, Emmanuel Picheau, Nicolas Chanut, Frédéric Nallet, Ahmed Bentaleb, Marie-Anne Dourges, Roland J. Pellenq, Elizabeth A. Hillard, Thierry Toupance, François Dole, Frédéric Louërat,* and Rénal Backov*

ABSTRACT: Alkylation of aromatic hydrocarbons is among the most industrially important reactions, employing acid catalysts such as $AlCl_3$, H_2SO_4, HF, or H_3PO_4. However, these catalysts present severe drawbacks, such as low selectivity and high corrosiveness. Taking advantage of the intrinsic high acid strength and Lewis and Brønsted acidity of niobium oxide, we have designed the first series of Nb_2O_5–SiO_2(HIPE) monolithic catalysts bearing multiscale porosity through the integration of a sol–gel process and the physical chemistry of complex fluids. The MUB-105 series offers efficient solvent-free heterogeneous catalysis toward Friedel–Crafts monoalkylation and -acylation reactions, where 100% conversion has been reached at 140 °C while cycling. Alkylation reactions employing the MUB-105(1) catalyst have a maximum turnover number (TON) of 104 and a turnover frequency (TOF) of 9 h^{-1}, whereas for acylation, MUB-105(1) and MUB-105(2) yield maximum TON and TOF values of 107 and 11 h^{-1}, respectively. Moreover, the catalysts are selective, producing equal amounts of ortho- and para-substituted alkylated products and greater than 90% of the para-substituted acylated product. The highest catalytic efficiencies are obtained for the MUB-105(1) catalyst, bearing the smallest Nb_2O_5 particle sizes, lowest Nb_2O_5 content, and the highest amorphous character. The catalysts presented here are in a monolithic self-standing state, offering easy handling, reusability, and separation from the final products.

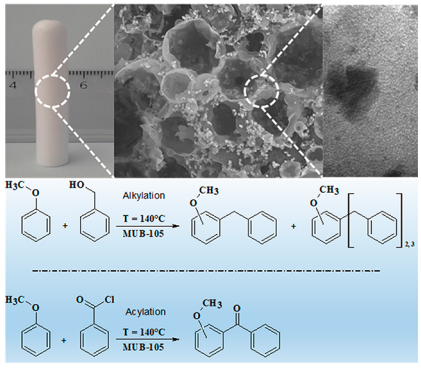

1. INTRODUCTION

Concentrated emulsions, whether direct (dispersion of oil-in-water) or reverse (dispersion of water-in-oil), when combined with the solidification of the continuous phase, can provide versatile monolithic porous materials presenting advanced functional properties.[1,2] In reverse emulsions, the hydrophobic continuous phase consists essentially of organic monomers, which can be polymerized to form organic poly(HIPE),[3] HIPE being the acronym for "high internal phase emulsion".[4] In direct emulsions, with a hydrophilic continuous phase, hydrolytic sol–gel processes can be implemented using hydrolyzed precursors.[5] As the emulsions must be stabilized by a surfactant above the critical micellar concentration (CMC), this last synthetic route offers hierarchical templating effects, namely, mesoporosity (pore diameters from 2 to 50 nm) arising from lyotrope mesophases and connected macroporosity (pore diameters above 50 nm) arising from the concentrated oil-in-water emulsions.[5] When the inorganic "glue" is silica, this inorganic polymer furthermore presents some microporosity (pore diameters below 2 nm) from the voids between the SiO_4 tetrahedrons.[6] These inorganic foams can be functionalized to generate heterogeneous catalysts.[7−9] For instance, when introducing titanium dioxide to the reaction mixture, random lasing properties[10−12] and photonic sponge catalysts for CO_2 photoreduction can be obtained,[13] whereas a mixture of alumina and silica generates efficient acidic heterogeneous catalysts.[14] In comparison to organic polyHIPE, studies on inorganic HIPE have been far less developed. The reason is that the inorganic skeleton shrinks during both the polycondensation step and the thermal treatment, making the fabrication of self-standing monolithic materials difficult. Even during the drying step, capillary forces have the tendency to induce cracks that impair the monolith cohesion. Recently, SB15-Si(HIPE) materials bearing a 2D-hexagonal mesoporous structure have been obtained with

KEYWORDS: sol–gel process, emulsion, hierarchical porous materials, integrative chemistry, heterogeneous catalysis

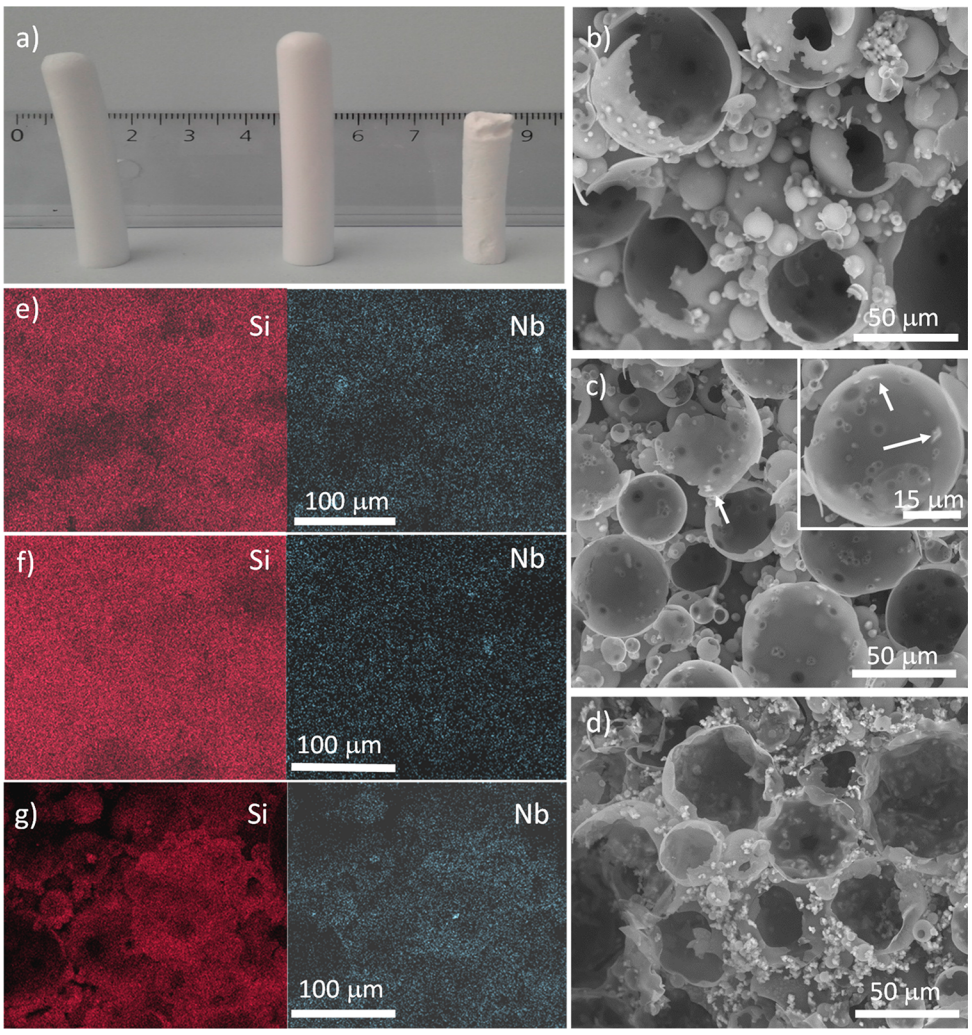

Figure 1. Observation of MUB-105(x) at the macroscopic length scale. (a) Self-standing niobium-based HIPE materials (from left to right) MUB-105(1), MUB-105(2), and MUB-105(3). (b–d) SEM images of (b) MUB-105(1), (c) MUB-105(2), and (d) MUB-105(3). (e–g) EDS images of (e) MUB-105(1), (f) MUB-105(2), and (g) MUB-105(3). The white arrows indicate submicrometer Nb_2O_5 crystals.

ammonium-based salts that favor the monolithic state via a kosmotrope effect.[15,16] Taking inspiration from this work, we here aim to develop novel inorganic foams, where a transition metal cation replaces the ammonium salt, retaining the kosmotrope effect and induces the generation of mixed oxide/HIPE monoliths. Niobium oxide is widely used in catalysis and in electrochromic and photoelectrochemical devices.[17,18] Hydrated niobium oxide ($Nb_2O_5{\cdot}nH_2O$) bears both a high acid strength (Hammett acidity (H_0) ≤ -5.6) and Lewis and Brønsted acidity. As such, it is of interest as a water-resistant solid acid catalyst for alkylation, esterification, hydrolysis, dehydration, and hydration reactions.[19,20] In this context, we report the syntheses of the first binary Nb_2O_5–SiO_2(HIPE) macro-mesocellular monolith, the MUB-105 series (MUB = Materials of the University of Bordeaux), their multiscale characterization, and their application toward the heterogeneous catalysis of the Friedel–Crafts alkylation and acylation of anisole.

2. EXPERIMENTAL SECTION

2.1. Material Synthesis. High-purity dodecane (≥99%), hydrochloric acid 37 wt % (HCl), tetraethylorthosilicate (≥99%, TEOS), niobium(II) pentachloride ($NbCl_5$), anisole, benzylic alcohol, and benzoyl chloride were purchased from Sigma-Aldrich. Tetradecyltrimethylammonium bromide (TTAB) was supplied by Alfa Aesar, whereas dichloromethane (CH_2Cl_2, ACS-reagent RPE) was purchased from Carlo Erba. All chemicals were used as received without any further purification. Deionized water was obtained using a Milli-Q water purification system

$NbCl_5$ (1.296, 0.648, or 0.324 g) was dissolved in 16 g of an aqueous TTAB (35 wt %) solution. HCl (37 wt %, 5 g) was added, followed by the addition of 5 g of TEOS (pH 0.05). The solution was stirred for 10 min to promote TEOS hydrolysis and allow the partial evaporation of the ethanol produced from the TEOS hydrolysis. Dodecane (37 g) was emulsified into the aqueous solution by dropwise addition into a mortar under manual stirring. The direct oil-in-water emulsion was then transferred to several hemolysis tubes employed as canisters, where the sol–gel process was left to proceed over 1 week at 25 °C. The solidified emulsions were then removed from the canisters and soaked for 12 h in dichloromethane. The wet materials were then allowed to slowly dry in a desiccator for 1 week and then in air during 3 days. Finally, a thermal treatment was applied to the materials to simultaneously sinter the silica network, calcine the TTAB surfactant employed as a mesoscopic mold, and promote the niobium oxide nucleation and growth. The thermal treatment was applied under atmospheric conditions as follows: a first temperature increase was applied at 2 °C/min to 180 °C with a 6 h plateau, followed by a second temperature ramp at 1 °C/min to 700 °C with a 6 h plateau. The cooling process was uncontrolled and directed by the oven inertia. The final self-standing monoliths were labeled MUB-

105(1) (0.324 g $NbCl_5$), MUB-105(2) (0.648 g $NbCl_5$), and MUB-105(3) (1.296 g $NbCl_5$) and are shown in Figure 1.

2.2. Catalytic Experiments. Alkylation reactions were carried out by stirring a suspension of the catalyst with a mixture of anisole (5.427 mL, 50 mmol) and benzylic alcohol (0.104 mL, 1 mmol) at 140 °C in a Reaction Station Carousel 12 Plus from Radleys. Once the MUB-105(x) catalyst was introduced into the solutions, the reaction media were placed under vacuum until the catalyst sank via replacement of air by the solution. The acylation experiments were undertaken using the same procedure as for the alkylation, using anisole (5.427 mL, 50 mmol) and benzoyl chloride (0.115 mL, 1 mmol). Catalytic activity and selectivity were measured by HPLC (HITACHI Chromaster with a Supercoil 5-C18 column at 30 °C and DAD detector at 258 nm; acetonitrile/water solution (60/40 V/V) mobile phase, flow rate of 1.0 mL min^{-1}) analysis of weighed samples of the reaction mixture diluted with ethanol (1.50 mL). Column chromatography purification was performed on silica gel Si 60 (40−63 μm, 230−400 mesh) with petroleum ether as eluent. ^1H and ^{13}C NMR spectra were recorded on a Jeol ECS-40 spectrometer, chemical shifts (δ) are given in parts per million relative to tetramethylsilane (TMS) as an internal standard. Mass spectra measurements were performed by CESAMO (Bordeaux, France).

2.3. Material Characterization. *2.3.1. Scanning Electron Microscopy (SEM).* The sample was properly broken down, crushed and fixed to an aluminum holder using silver paint. The fractured surface was metalized with gold/palladium sputtering. SEM images were acquired with a Hitachi TM-1000 tabletop scanning electron microscope operating with a 15 kV accelerating voltage. Energy-dispersive X-ray spectroscopy (EDS) spectra and maps were obtained on a ZEISS EVO 50 scanning electron microscope equipped with an EDX EDAX detector. The electronic source was a lanthanum hexaboride tip (LaB_6) and the accelerating voltage was 20 kV.

2.3.2. Wide-Angle X-ray Scattering (WAXS). X-ray measurements were done on a Rigaku Nanoviewer (XRF microsource generator, MicroMax 007HF), with a rotating anode coupled to a confocal Max-Flux Osmic mirror (Applied Rigaku Technolgies, Austin, USA), producing a beam of 1.5418 Å (8 keV). A wide-angle X-ray scattering with transmission geometry setting was chosen. Samples were put in a 1.5 mm diameter glass capillary (Glaskapillaren GLAS, Glas-Technik & Konstruktion, Schönwalde-Glien, Germany) with a sample−detector distance of 125 mm providing access to angles in the 3−53° range. Images were collected on a MAR345 image plate detector (MARResearch, Norderstedt, Germany) and spectra were integrated with *FIT2D* software (ERSF; http://www.esrf.eu/).

2.3.3. Small-Angle X-ray Scattering (SAXS). X-ray diffraction experiments were done on a XEUSS 2.0 device (XENOCS, Grenoble, France) with a GeniX3D system (XENOCS microfocus copper anode source coupled to a FOX3D single reflection mirror) delivering a monochromatic 8 keV beam (Cu Kα, λ = 1.5418 Å). The beam was further collimated by a set of 2 motorized, scatter-less (4-blade) slits. The powdered samples were put into thin glass capillaries (optical path of ∼1.5 mm) and exposed for typically 2 h when recording single images and twice this duration for composite images recorded in the so-called "virtual detector" mode. Data were collected by a two-dimensional DECTRIS PILATUS-300k detector (Baden-Dättwill, Switzerland) placed at a sample-to-detector distance of 1635 mm (calibrated with a silver behenate standard), giving access to a range of scattering wave vectors q between 0.007 A^{-1} and 0.23 A^{-1} in standard mode, extended to 0.38 A^{-1} in the "virtual detector" mode. Note that the XEUSS 2.0 device offers a wholly evacuated flight path, from the downstream end of the mirror to a few centimeters before the detector, including the samples. The 1D diffractograms (intensity I vs q) were obtained by processing the detector images with FOXTROT software (collaboration between XENOCS and the SOLEIL synchrotron (Gif-sur-Yvette, France) SWING beamline team).

2.3.4. Transmission Electron Microscopy (TEM). The samples were ground in a mortar then dissolved in ethanol. A drop of the solution was placed and dried on a TEM copper grid covered with carbon film. The TEM pictures were obtained with a Hitachi H7650 TEM operating at 80 kV.

2.3.5. Raman Spectroscopy. Raman Spectroscopy was performed on a Horiba Jobin Yvon XploRA Raman microspectrometer, Olympus 50X LWD objective, with a 532 nm (2.33 eV) excitation wavelength (laser spot size ∼1 μm), calibrated with SiO_2 (TO mode). Spectra were acquired with a cooled Andor CCD detector, using a 1200 line per mm grating and 120 s acquisition time, with the laser filtered to 25% of its maximal power (∼14 mW).

2.3.6. Gas Sorption Measurements. A Micromeritics 3Flex surface characterization analyzer (Micromeritics Instrument Corp, Norcross, GA) was used for all measurements. Prior to measurement, the samples were activated under a secondary vacuum at 110 °C for 12 h. Activation at 350 °C for 12 h was also performed for comparison and led to similar results, indicating that the outgassing procedure was efficient for both temperatures. Nitrogen (N_2) adsorption isotherms measured at 77 K and argon (Ar) adsorption isotherms measured at 87 K were collected and interpreted using a multipoint Brunauer−Emmett−Teller (BET) analysis for surface area determination[21] over a 0.05−0.30 relative pressure range (P/P_0) and with a N_2 and Ar cross-section of 0.162 and 0.143 nm^2, respectively. The mesoporous surface area was determined using the Barrett, Joyner, and Halenda (BJH) method, whereas the microporous surface area was estimated by the difference between the BJH mesoporous surface area and the BET surface area, assuming that the macroporous surface area is negligible.

2.3.7. Mercury Porosimetry. Intrusion/extrusion mercury measurements were performed using a Micromeritics Autopore IV apparatus to determine the scaffolds' macrocellular characteristics.

2.3.8. Helium Pycnometry. Material skeleton densities were determined through helium pycnometry using a Micromeritics AccuPy 1330 apparatus. The samples were degassed under vacuum at 130 °C for 12 h prior performing the measurement.

2.3.9. Elemental Analyses. Elemental analyses were performed by ICP with ICP AES iCAP 6500 DUO and ICP AES iCAP 7400 Radia apparatuses.

2.3.10. Thermogravimetric Analysis (TGA). TGA was performed in air using a TGA 5500 Discovery TA apparatus with a heating rate of 5 °C min^{-1}.

2.3.11. NH_3-TPD (Temperature-Programmed Desorption). The acidic strength was analyzed with a Micromeritics Autochem II 2920 apparatus. A first He (30 mL min^{-1}) pretreatment was performed at 600 °C for 1 h (heating rate 10 °C min^{-1}). The NH_3 adsorption was performed at 100 °C (5 vol % NH_3/He) at 30 mL min^{-1} for 30 min. A He purge was imposed at 30 mL min^{-1} for 2 h at 100 °C. Finally, NH_3 thermodesorption was estimated from 100 to 600 °C (heating rate of 5 °C min^{-1}) with a 1 h plateau at 600 °C.

2.3.12. XPS. XPS surface analyses were performed on powdered samples with an ESCALAB 220 i-XL apparatus using a non-monochromatized Mg source (10 mA × 12 kV). The analyzed area was 150 μm in diameter. The full spectra (0 to 1100 eV) were obtained with a constant pass energy of 200 eV and high-resolution spectra with a constant pass energy of 20 eV. Charge neutralization was applied during analysis. High-resolution spectra (i.e., C 1s, O 1s, and Nb 3d) were fitted using the *AVANTAGE* software provided by ThermoFisher Scientific (all spectra shifted versus Si 2p at 103.4 eV as expected for SiO_2 and Scofield sensitivity factors used for quantification).

3. RESULTS AND DISCUSSION

3.1. Materials Characterization at the Macroscopic Length Scale. The MUB-105(x) series were obtained as monolithic materials whatever the niobium content (Figure 1a). The macroporosity induced through the departure of the oil droplets in the starting direct emulsions (Figure 1b−d) resembles typical aggregated hollow spheres when compared with traditional Si(HIPE).[5] In MUB-105(2) and MUB-105(3), tiny crystals are observed at the surface of the macroscopic

Table 1. Elemental Analysis and TGA Data for Determination of Molar Weight (MW) and Stoichiometry

	Nb wt %		Si wt %		H_2O wt %			
sample	found	calcd	found	calcd	found[a]	calcd	MW (g mol^{-1})	stoichiometry
MUB-105(1)	5.20	5.18	35.5	34.85	17.5	16.8	80.37	$(Nb_2O_5)_{0.0225}$ $(SiO_{1.95}(OH)_{0.1})_{1.0}$. 0.75 H_2O
MUB-105(2)	6.38	6.30	35.45	31.60	23.10	22.34	88.66	$(Nb_2O_5)_{0.03}$ $(SiO_{1.95}(OH)_{0.1})_{1.0}$. 1.1 H_2O
MUB-105(3)	17.50	16.92	31.01	30.40	11.95	11.30	92.72	$(Nb_2O_5)_{0.084}$ $(SiO_2)_{1.0}$. 0.58 H_2O

[a]H_2O wt% determined by TGA under air at a heating rate of 5 °C/min (Figure S1). Elemental analyses were performed using ICP for niobium and silicon wt % determinations.

walls (Plateau borders), which have the tendency to increase both in number and size when the Nb_2O_5 content employed during the syntheses is increased (Figure 1c, d). In MUB-105(1), which contains the lowest amount of Nb_2O_5 (Table 1), no crystals were observed by SEM. This does not mean that Nb_2O_5 is absent, but that the crystals (as observed later by TEM) are too small to be distinguished at the SEM scale. EDS investigation (Figure 1e–g) shows that the niobium distribution in the silica is rather homogeneous within the material core. The niobium EDS intensity increases with increasing quantity of Nb_2O_5 used in the reaction from MUB-105(1) to MUB-105(3).

Because of the coalescence of the droplets and the network shrinkage during sol–gel polycondensation and the heat-induced sintering process, we can observe connecting windows/apertures on the macroscopic walls showing open macro-porosity (Figure 1b–d). Beyond this SEM information, the porosity of the MUB-105 series was assessed by combining mercury intrusion porosimetry for the determination of the bulk density (Figure 2), and helium (He) pycnometry for the

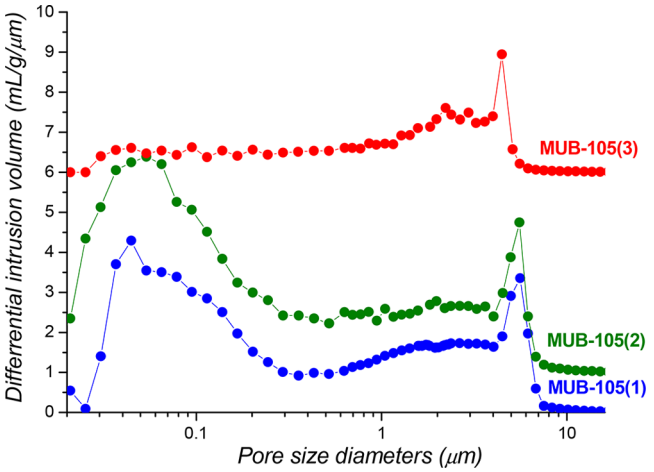

Figure 2. Pore size distribution obtained through mercury porosimetry. MUB-105(1) blue dots, MUB-105(2) green dots, and MUB-105(3) red dots. For the sake of clarity, the MUB-105(2) and the MUB-105(3) curves have been offset by 1.0 and 6.0 mL/(g μm), respectively.

determination of the skeleton density (Table 2). The porosity percentage was then calculated using eq 1.

$$\%\text{porosity} = [(1 - (\text{bulk density}/\text{skeleton density})]100 \quad (1)$$

As shown in Table 2, the MUB-105(x) materials present a porosity around 97% for all samples. With increasing amounts of niobium, the bulk densities almost double from the MUB-105(1) and MUB-105(2) to the MUB-105(3) samples, in

Table 2. Bulk Density Measured by Mercury Intrusion Porosimetry, Skeleton Density Measured by Helium Pycnometry and Calculated Porosity Using Eq 1

sample	porosity (%)	skeleton density (g cm^{-3})	bulk density (g cm^{-3})
Si(HIPE)	96 ± 1%	2.22 ± 0.02	0.085 ± 0.005
MUB-105(1)	97 ± 1%	2.24 ± 0.02	0.070 ± 0.005
MUB-105(2)	97 ± 1%	2.32 ± 0.02	0.070 ± 0.005
MUB-105(3)	95 ± 1%	2.52 ± 0.02	0.118 ± 0.005

agreement with the fact that the niobium weight percent increases respectively from 5 to 6 to 17 wt % (Table 1).

When considering Figure 2, we emphasize that the pore size distributions obtained by mercury porosimetry correspond to the areas that restrict the mercury intrusion, that is to say, the connecting cell-junctions, seen in Figure 1b–d. As is typical for Si(HIPE) materials,[5,15,16] the cell junctions are rather disparate in diameter, ranging from 0.081 to 7 μm with a tendency to express a bimodal character, this feature being clearest for MUB-105(1) and MUB-105(2). In MUB-105(3), bearing the biggest Nb_2O_5 particles (Figure 1d), the lack of recorded submicrometer porosity may be due to blockage of the smallest connecting windows.

3.2. Materials Characterization at the Mesoscopic Length Scale. To obtain further insight into the nature of the porosity of the MUB-105(x) series, we performed argon adsorption at 87 K and nitrogen adsorption at 77 K for surface-area determination (Figure 3). All the isotherms show some gas uptake at low relative pressure, highlighting the presence of micropores (<2 nm) in the samples. Additionally, a narrow hysteresis loop between the adsorption and desorption branches in the relative pressure range of 0.4–0.6 can be observed, highlighting the presence of small mesopores in the samples (pores between 2 and 5 nm based on BJH analysis of the adsorption branch). We also note an increase in the adsorbed volume in all the adsorption isotherms at high relative pressure, which demonstrates the material's macro-porosity. As shown in Table 3, the BET surface areas are comparable when using both Ar and N_2. However, the microporous surface area measured by N_2 is much more significant in comparison to that determined using Ar. This can be explained by the quadrupolar nature of the N_2 molecules, which induces specific interactions with surface functional groups and is at the origin of the observed virtual increase in microporous surface area. Indeed, it is well-known that these specific interactions strongly affect the micropore filling pressure, so that the pore filling pressure is not strictly correlated with the pore size.

In contrast to N_2, Ar does not display specific interactions with surface functional groups, thus allowing for a much more precise surface area determination for samples bearing oxides and pendant OH groups. For these reasons, and following the

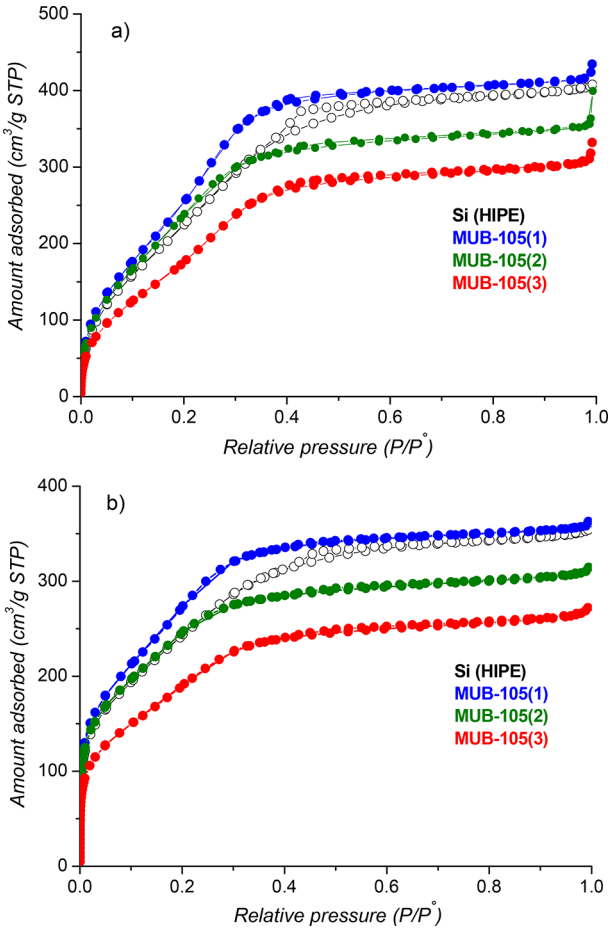

Figure 3. (a) Argon adsorption isotherm measured at 87 K and (b) N_2 adsorption isotherm measured at 77 K for unmodified Si(HIPE) and the MUB series. White, blue, green, and red full circles correspond to Si(HIPE), MUB-105(1), MUB-105(2), and MUB-105(3), respectively.

guidelines of the 2015 IUPAC physisorption of gases recommendations report, the results obtained with Ar will be used here. We can notice that surface area obtained through Ar physisorption measurements slightly decreases from Si(HIPE) to MUB-105(3), in agreement with the increase in skeleton density (Table 2). This trend is not observed when comparing Si(HIPE) with MUB-105(1) and MUB-105(2), particularly for the MUB-105(1) where it increases from 874 to 1095 $m^2.g^{-1}$ (Table 3). As revealed later with SAXS experiments, we do not observe a drastic variation of the mesoporous organization of the silica support when considering either the Si(HIPE) and the MUB-105 series, including MUB-105(1). Therefore, the above-mentioned increase of surface area cannot be explained by specific chaotrope-kosmotrope synergetic effects between the silica precursors and $NbCl_2{\cdot}6\ H_2O$ salts,[15] but rather by an additional surface area generated by the presence of finely divided niobium nanoparticles in the MUB-105(1) sample. This interpretation is indeed supported by TEM investigations (Figure 4).

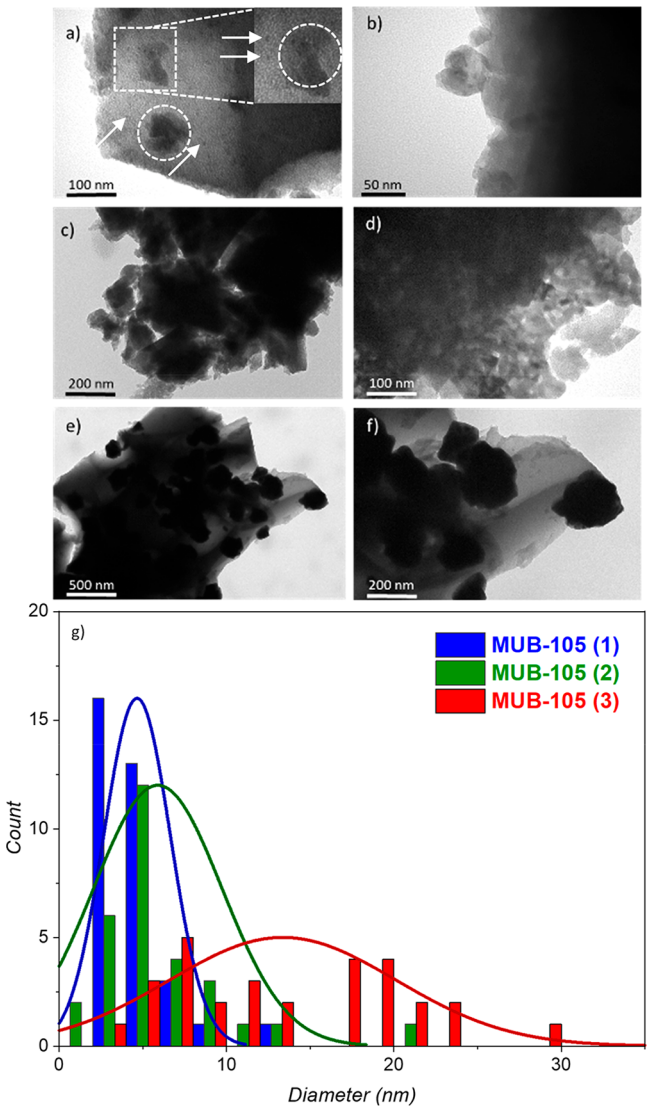

Figure 4. Investigation at the mesoscopic length scale through TEM. (a, b) MUB-105(1), (c, d) MUB-105(2), and (e, f) MUB-105(3), (g) Nb_2O_5 primary crystallite size deconvolution using the *ImageJ* program. White circles show Nb_2O_5 aggregated crystals and white arrows show isolated crystals. The continuous gray scale represents the siliceous continuous phase. An average of 5 μm^2 has been investigated for each samples.

In Figure 4, we can notice that the Nb_2O_5 primary particle size increases from MUB-105(1) to MUB-105(3), particularly evidenced by the particle size deconvolution (Figure 4g). For MUB-105(2) and MUB-105(3), the particles are aggregated

Table 3. Surface Areas Determined Using Both N_2 and Ar

sample	N_2-BET ($m^2\ g^{-1}$)	Ar-BET ($m^2\ g^{-1}$)	S_{micro} (N_2) ($m^2\ g^{-1}$)	S_{meso} (N_2) ($m^2\ g^{-1}$)	S_{micro} (Ar) ($m^2\ g^{-1}$)	S_{meso} (Ar) ($m^2\ g^{-1}$)
Si(HIPE)	930	874	425	505	271	603
MUB-105(1)	1092	1095	604	488	320	775
MUB-105(2)	940	945	620	320	210	735
MUB-105(3)	745	730	367	378	185	545

where aggregate size falls in the range of 50 nm (Figure 4c, d) to 200 nm (Figure 4e, f), the biggest particles being also visible with SEM (Figure 1c, d). This is not the case for MUB-105(1) where no Nb_2O_5 crystals were observed at the SEM scale despite a good niobium dispersion revealed by EDS (Figure 1e). Indeed, in Figure 4 a, b we can see that the niobium oxide nanoparticles are highly divided, with sizes centered at 5 nm (Figure 4g), and with limited aggregation. As such, when quantifying the specific surface area of MUB-105(1), we must add the external surface area of the niobium nanocrystals to the specific surface area emerging from the micro-mesporosity of the silica support. This suggests that the nanoparticles are not embedded within the mesoscopic voids; this would induce a decrease of the surface area, which is not the case. Indeed, SAXS further supports the structural mesoscopic description reached by TEM. As shown in Figure 5, the small-angle regime

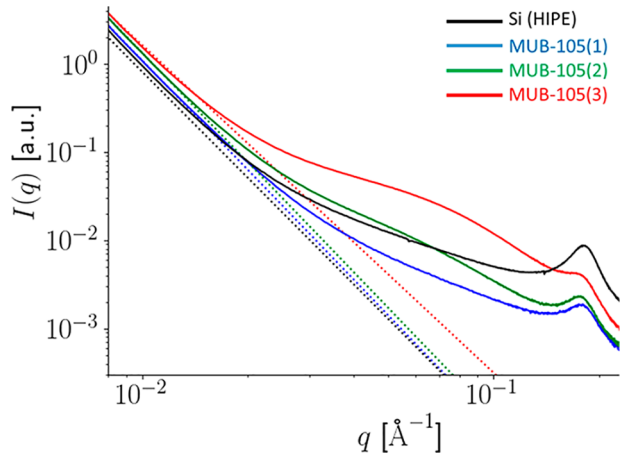

Figure 5. Small-angle scattering intensities (double logarithmic scale) for the reference Si-(HIPE) (black), MUB-105(1) (blue), MUB-105(2) (green), and MUB-105(3) (red). The colored dotted lines correspond to power-law decaying intensities with exponents close to −4 (Porod's law) except for the MUB-105(3) sample, where the exponent is slightly larger, approximately −3.7.

of the scattering intensity data exhibits the expected power-law decay with an exponent of −4 (Porod's law), characteristic[23] of clear-cut interfaces—here separating an "outer" empty medium (air) from an "inner" filled medium (silica).

The modest but significant departure from Porod's law, namely, an initial decay tentatively described by a power-law with an exponent of −3.7 observed in the MUB-105(3) sample, is attributed to the presence of numerous niobium-rich nanocrystals segregated from the silica matrix, as suggested by the TEM data (Figure 4e, f) and skeleton densities (Table 2). The structural peak at q^*, associated with the mesoscopic structure of the concentrated worm-like micellar phase prepared during synthesis, is always found in the calcined materials, as is especially clear in the Porod representation used in Figure 6. The extracted structural parameters, derived from $2\pi/q^*$, are 3.38, 3.40, 3.45, and 3.43 nm, for Si(HIPE), MUB-105(1), MUB-105(2), and MUB-105(3), respectively. This information is indeed very significant, as these mesoscopic void parameters are smaller than the nanoparticles observed in TEM, even for the MUB-105(1), bearing the smallest nanoparticles. This means that the nanoparticles seen in the TEM images are not embedded within the silica mesoscopic

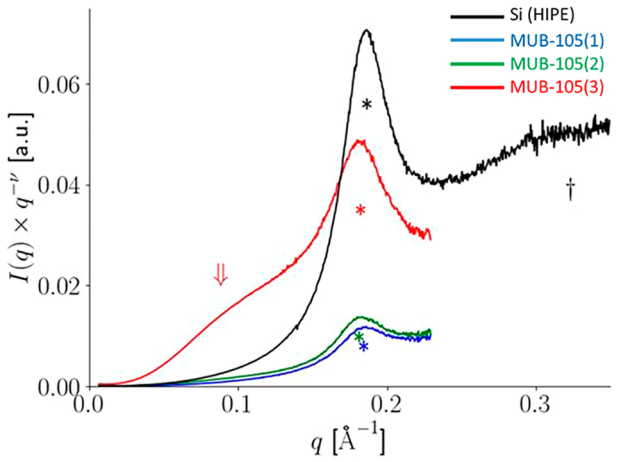

Figure 6. Porod-like representation of the small-angle intensities scattered by the calcined materials, emphasizing the mesoporous structure of the reference SI-(HIPE) sample (black) and the three MUB-105(1) (blue), MUB-105(2) (green), and MUB-105(3) (red) samples. Exponents ν close to −4 as expected from Porod's law, except for the MUB-105(3) sample, where its value is slightly larger, approximately −3.7. The colored star marks the location q^* in reciprocal space of the characteristic structural peak from the concentrated worm-like micellar phase used during synthesis. Note that for the reference Si-(HIPE) sample, a "second-order" peak may be found at roughly $\sqrt{3}$ times the "first order" peak (†), as expected for hexagonal 2D order. Note the presence of a broad feature at about $2\pi/70$ Å^{-1} (downward double arrow symbol) in MUB-105(3), possibly associated with Nb_2O_5 nanocrystals.

voids but rather randomly dispersed within the silica walls (Plateau borders), both in the bulk and on the surface.

3.3. Materials Characterization at the Microscopic Length Scale. To probe the microscopic length scale, we have performed WAXS investigations (Figure 7). It is well-known

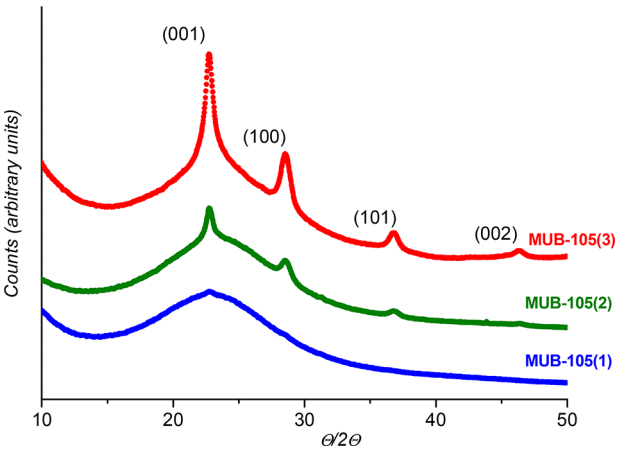

Figure 7. WAXS investigation. MUB-105(1) blue dots, MUB-105(2) green dots, and MUB-10((3) red dots. Main diffraction peaks of the Nb_2O_5 pseudohexagonal TT-Nb_2O_5 (JCPDS 28-317).

that niobium oxide adopts different allotropic forms depending on the heat treatment applied. At low temperature, amorphous niobium oxide, $Nb_2O_5{\cdot}nH_2O$, possesses distorted NbO_6 octahedra, NbO_7 pentagonal bipyramids, and NbO_8 hexagonal bipyramids as structural units.[24,25] Increasing the temperature (300−500 °C) promotes pseudohexagonal niobium oxide (TT-Nb_2O_5), whereas orthorhombic T-Nb_2O_5 is reached at

700−800 °C and monoclinic H-Nb_2O_5 at temperatures higher than 1000 °C.

Considering that the MUB-105 series was treated at 700 °C, the orthorhombic phase (T-Nb_2O_5) should have been obtained. However, Figure 7 shows that the less crystalline pseudohexagonal TT-Nb_2O_5 phase was obtained in all cases, where the diffraction peak intensity increases with the increasing amounts of TT-Nb_2O_5 present within the materials. Indeed, it has been already shown that amorphous silica hinders Nb_2O_5 thermo-induced crystallization.[26,27] When a strong interaction is established via Nb−O−Si bonds, only the amorphous form of Nb_2O_5 is present after a thermal treatment at 500 °C for 2 h, whereas only weak diffraction peaks of the TT-Nb_2O_5 phase appeared when treated at 1000 °C for at least 48 h.[28] The tendency to retain an amorphous character is indeed very important, as higher temperatures and crystallinity are associated with a decrease in the catalytic activity of both the solid Brønsted acid and the surface area.[29] Protonation, providing the Brønsted acid sites, is suppressed in the ordered crystalline structure but favored in the distorted polyhedra in amorphous $Nb_2O_5{\cdot}nH_2O$. The distorted polyhedron can be identified in Raman spectroscopy, which was performed to confirm the niobium oxide structure (Figure 8).

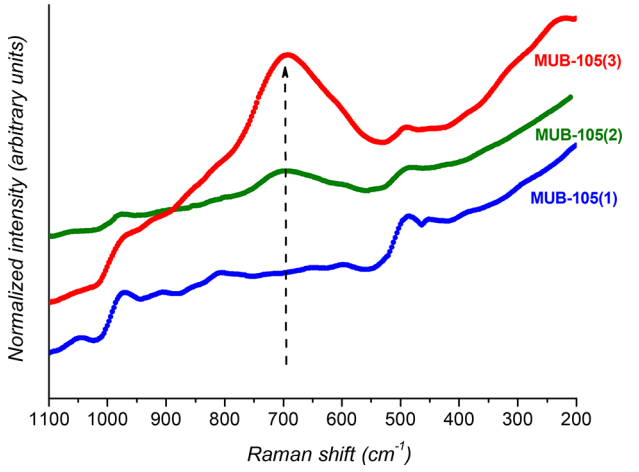

Figure 8. Raman spectra of the MUB-105(x) series. The dashed line is aligned at 696 cm^{-1}. MUB-105(1), blue dots; MUB-105(2), green dots; and MUB-105(3), red dots.

The wide Raman band in the 550−800 cm^{-1} region, intensifying from MUB-105(1) to MUB-105(3) as the Nb_2O_5 content increases (Table 1), is assigned to the symmetric stretching modes of slightly distorted NbO_6 octahedra, while the associated bending modes of Nb−O−Nb appear in the low energy region around 200 cm^{-1}.[29,30] In the case of pseudohexagonal Nb_2O_5 (TT phase), the Raman band of the symmetric stretching modes of the NbO_6 octahedra is observed at around 700 cm^{-1}. We notice that this peak is rather broad, implying that both the MUB-105(2) and MUB-105(3) samples contain distorted NbO_6 octahedra, NbO_7 pentagonal bipyramids, and NbO_8 hexagonal bipyramids.[29] As MUB-105(1) bears the lowest Nb wt %, the Raman Nb_2O_5 specific modes are rather difficult to assess. On the contrary, MUB-105(1) displays some Raman modes characteristic of amorphous silica, which diminish as the Nb_2O_5 content increases. We can first notice a rather intense band located around 975 cm^{-1} due to symmetric silanol stretches in the Si−OH groups. Around 800 cm^{-1}, a Raman mode is present because of the bending vibration parallel to the bisector of the Si−O−Si angle. Centered at 600 cm^{-1}, we can observe the Raman D2 mode characteristic of the ring breathing of three-membered siloxane rings. A sharpened broad band that couples the symmetric oxygen stretch of three network oxygen atoms connected to a silicon atom that has become decoupled from the network via a terminating hydroxyl group (D0), as well as the (D1) band addressing the ring breathing of four-membered siloxane rings, at the lowest frequencies was found at 450−500 cm^{-1}.[31]

Both the strength and concentration of the acidity existing on the catalyst supports were estimated by NH_3-TPD. NH_3 being basic, its ability to selectively adsorb on different sites (weak, medium, and strong), and its small kinetic diameter (0.26 nm) make it a useful probe molecule to provide comparative details about the surface acidity of the catalysts. The NH_3-TPD curves can be found in Figure S2. The surface acidic concentration increases from 0.00 to 12, 73, and 410 μmol/g, respectively, for Si(HIPE) (containing silanol groups but free of Nb_2O_5 nanocrystals) to MUB-105(3), MUB-105(2), and MUB-105(1). If the acidic site concentration drastically increases from MUB-105(3) to MUB-105(1), the acidic strength slightly decreases where the maximum NH_3 desorption switches from 200 to 270 and 325 °C, respectively, for the MUB-105(1) to the MUB-105(2) and MUB-105(3) (Figure S2).[32]

To relate the acidic strength to the Nb oxidation state, XPS investigations have been performed prior to use in catalysis. Except for a C 1s feature, which can be assigned to adventitious carbon species, only niobium (Nb 3d, Nb 3p), silicon (Si 2p, Si 2s) and oxygen (O1s) spectra were detected in the survey of the MUB-105(3) materials (Figure 9, Table S1).

The Nb 3d region showed two components with binding energy maxima located at 207.4 ± 0.1 and 210.1 eV ± 0.1 eV that can be assigned to the Nb $3d_{5/2}$ and $Nb3d_{3/2}$ core level binding energies. These energy values, along with the spin−orbit separation of 2.7 ± 0.1 eV, are in good agreement with those reported for Nb(V) sites in Nb_2O_5.[33,34] In addition, no feature can be observed in the 204−200 eV range, ruling out the presence of any Nb(II) or Nb(0) species.[35] Furthermore, the O 1s spectrum exhibits a main feature at 532.6 ± 0.1 eV, which can be attributed to the lattice oxygen O^{2-} in silica, and two minor ones at 530.3 ± 0.1 eV and 533.6 ± 0.1 eV, which can be attributed to the lattice oxygen O^{2-} in niobium oxide and O−C species, respectively. XPS investigations for MUB-105(1) and MUB-105(2) revealed similar features and conclusions (Figures S3 and S4). As expected, an increase in the surface niobium content was observed from MUB-105(1) to MUB-105(3) (Table S2). All these features clearly confirm the presence of Nb_2O_5 in each sample, where niobium mainly exists in the 5+ oxidation state. Nonetheless, the signal-to-noise ratio is too low to correlate the acidic strength evolution with changes in the oxidation state of niobium sites.

3.4. Alkylation and Acylation-Based Heterogeneous Catalysis. Alkylation of aromatic hydrocarbons is one of the most important catalytic reactions used at the industrial scale. This process employs acid catalysts such as $AlCl_3$, H_2SO_4, HF or H_3PO_4, despite their intrinsic drawbacks of low selectivity and high corrosiveness.[36] To circumvent these weaknesses, the deposition of niobium oxide on the surface of a suitable support, bearing a large surface area and easily controlled

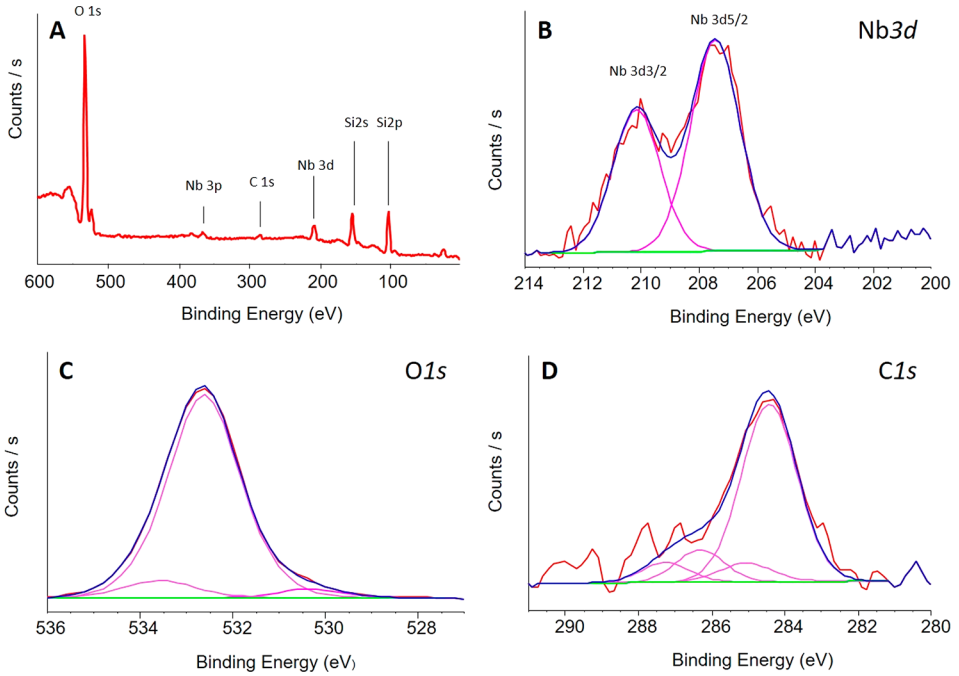

Figure 9. XPS analysis of MUB-105(3) sample: (A) XPS survey 0−600 eV, (B) Nb 3d region, (C) O 1s region, and (D) C 1s region.

Scheme 1. Possible Products in Alkylation or Acylation of Anisole with Benzyl Alcohol or Benzoyl Chloride, Respectively[a]

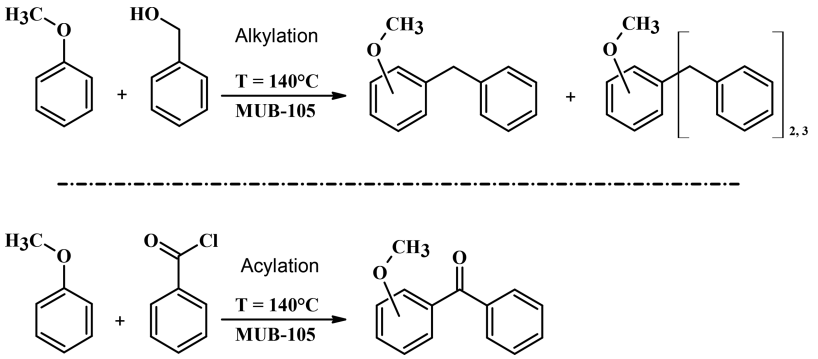

[a]The expected products are isomers of benzyl anisole, the di (tri) substituted, and optionally, the dehydration of the benzyl alcohol molecules for the alkylation reaction or isomers of methoxybenzophenones for the acylation reaction. Without a catalyst, the reactions exhibit no activity.

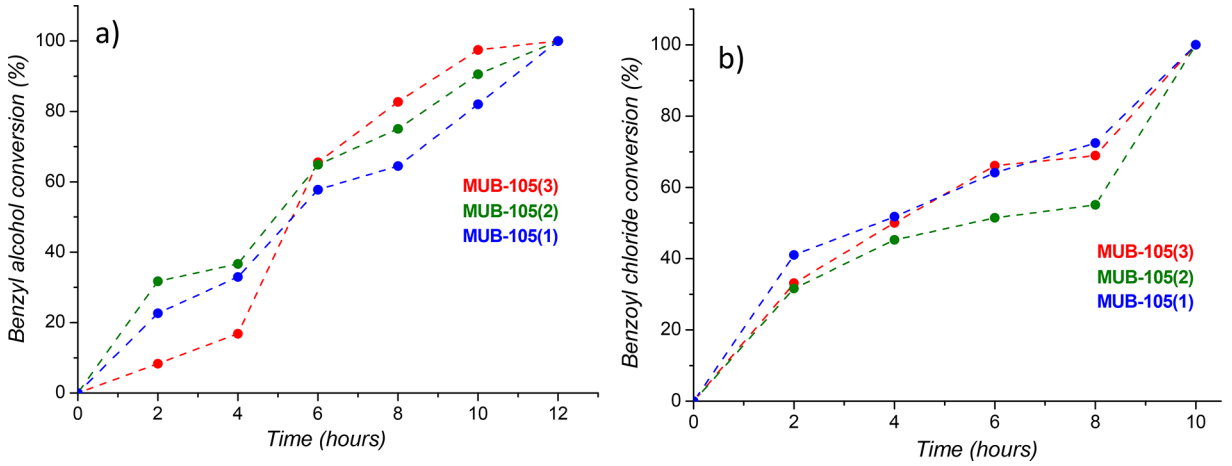

Figure 10. Apparent conversion kinetics of (a) benzyl anisole (alkylation) and (b) benzoyl chloride (acylation). MUB-105(1), blue dots; MUB-105(2), green dots' and MUB-105(3), red dots.

textural properties, is an interesting possibility.[37] Here we have performed solvent-free Friedel−Crafts alkylation reactions, and have extended the catalytic experiments to acylation reactions where, to the best of our knowledge, monophasic supported-niobium oxide has been employed for the first time (Scheme 1).

Considering the solvent-free alkylation reaction, the first important result is the rather high selectivity of the MUB-105(x) catalysts. Indeed, when analyzing the reaction products by LC/MS and ^{1}H NMR, we find only the monoalkylated ortho- and para-benzyl anisole in a ratio of 50/50 mol % (Figures S5 and S6). Unlike other studies,[38−40] we did not obtain a statistical 67/33 mol % ortho/para proportion, the selectivity in the present experiments being more directed toward the para-alkylated product. Nor did we observe any dehydration byproducts, or poly alkylated byproducts, contrary to de La Cruza et al.[40] Examples of conversion kinetics for the alkylation and acylation reactions are proposed in Figure 10. The three MUB-105(x) catalysts present the same activity profile, where the conversions reach 100% at 12 h for alkylation and 10 h for acylation (Figure 10). The similar conversion kinetic profiles (Figure 10), despite the varying amount of Nb_2O_5 catalytic sites (Table 1), indicate that the kinetics are controlled by the monolithic nature of the catalysts employed in batch mode, where both reactants and products must diffuse into or out of the monoliths. This is why the kinetics depicted in Figure 10 are only "apparent" kinetic profiles.

The results for the alkylation reaction of anisole with benzyl alcohol are presented in Table 4.

Table 4. Conversion for Anisole Alkylation with Benzyl Alcohol

entry	catalyst	mass (mg)	time (h)	run	conversion[a] (%)
1	none		12	1	<5
2	Si(HIPE)	25.8	12	1	6
3	Nb_2O_5	31.2	12	1	8
4	MUB-105(3)	29.9	12	1	100 (46/51)[b]
5−10	MUB-105(3)	27.9	12	2−7	100
11	MUB-105(3)	27.9	12	8	80
12	MUB-105(3)	27.9	24	8	100
13	MUB-105(3)	26.6	12	9	75
14−21	MUB-105(2)	39.3	12	1−8	100 (46/50)[b]
22	MUB-105(2)	28.5	12	9	85
23	MUB-105(1)	27.9	12	1	100 (44/47)[b]
24−31	MUB-105(1)	34.2	12	2−8	100
32	MUB-105(1)	34.2	12	9	63

[a]The solutions were analyzed during the reactions through HPLC. Anisole, (50 mmol), benzylic alcohol (1 mmol), MUB-105(x), T = 140 °C. [b]Isolated yields of pure products obtained by column chromatography; selectivity (ortho/para).

Under the experimental procedure employed here (140 °C, no solvent, atmospheric pressure), no reaction takes place in the absence of the catalyst (Table 4, entry 1). The same can be stated for commercial Nb_2O_5 or niobium-free Si-(HIPE) (Table 4, entries 2 and 3). In contrast, when the reaction is catalyzed by MUB-105(x), the conversions reach 100% after 12 h. The catalysts are extremely efficient regarding anisole alkylation with benzylic alcohol and very selective toward benzyl-anisole monoalkylation production (entry 4), with the selectivities toward the ortho/para-substituted products indicated in parentheses, (Table 4 entry 4, 14−21, 24−31). For instance, we repeatedly added the same quantity of alcohol, up to 7 fold, to the MUB-105(3) catalyst, reaching a 100% conversion yield (Table 4, entries 4−10). The alkylation conversion using MUB-105(3) decreases to 80% after 8 runs (entry 11), but total conversion is still reached in 1 day (Table 4, entry 12). Varying the batch when using the monolithic system is simple, as either the reaction media or the catalyst can be removed from the reactor without any phase separation procedure (sedimentation, filtration and so forth). As the catalyst is a self-standing monolith, it can be regenerated by thermal treatment at 700 °C (the same treatment as in the synthetic procedure). The niobium oxide nanoparticles, being dispersed within the silica matrices, cannot sinter, and consequently, we recover the 100% conversion yield after thermal treatment. These observations are similar for the MUB-105(2) and MUB-105(1) catalysts, which are slightly more efficient, as up to 8 equiv. of alcohol was repetitively added to the same batch with 100% conversion yield (Table 4, entries 14−22 and 23−32).

In the catalytic experiments, we used only 30 mg of MUB-105(x) compared to 200 mg of unsupported HNb_3O_8 exfoliated sheets (yield 95.6%),[38] 100 mg of unsupported Nb_2O_5 powder[39] (yield 100%), and 1 g of alumina-supported Nb_2O_5 powder (yield 100%),[40] for the same reactant concentrations and an applied temperature of 140 °C (as opposed to 150 °C,[38] 100 °C,[39] and reflux (154 °C),[40] respectively.) The present conversions were slower, with full conversions in 12 h, whereas 95.6% conversion was obtained in 4 h with HNb_3O_8 sheets[38] and a full conversion in 90 min for alumina-supported Nb_2O_5.[40] This is likely due to the lower Nb_2O_5 content employed here, in addition to the monolithic character. As the catalytic conditions vary from one experiment to another, it is difficult to compare the catalytic efficiencies, bearing in mind that a conversion yield does not reflect the intrinsic catalytic efficiency, particularly if the catalyst content is overexpressed. What really depicts the catalyst efficiency is rather the ability to cycle, with a minimal catalyst content, quantified by turnover numbers (TON) and turnover frequencies (TOF). Details of the calculations of these metrics are provided in the Supporting Information. In Table 5, we note that MUB-105(1) possesses a TON of 836 and a TOF of 9 h^{-1} for the alkylation reaction, 20 and two times higher, respectively, than those found in the literature,[38−40] while at the same time offering easy separation from both the reaction media and final products and simple regeneration through thermal treatment.

Table 5. Catalysts Turnover Numbers (TON) and Turn Over Frequencies (TOF)[a]

	alkylation		acylation	
catalysts	TON*	TOF* (h^{-1})	TON*	TOF* (h^{-1})
MUB-105(3)	295 (323)	3 (3)	379 (417)	5 (5)
MUB-105(2)	830 (918)	9 (8)	1010 (1107)	13 (12)
MUB-105(1)	836 (901)	9 (8)	919 (1028)	11 (1)

[a]TON and TOF are calculated here while considering the addition of runs reaching 100% conversion and not the addition of runs to render the catalyst completely inactive. The numbers in brackets are those taking into account all cycles.

To explore the MUB-105(x) versatility, we also tested them in acylation reactions. To the best of our knowledge, this is the first time that monophasic Nb_2O_5-based catalysts have been used for acylation. We used the same experimental procedure (140 °C, no solvent, atmospheric pressure) as for the alkylation reaction, and find that total conversion is reached in 10 h (Figure 9b). In comparison, there is no reaction without the catalyst, (Table 6, entry 1), whereas commercial

Table 6. Conversion Yields for Anisole Acylation with Benzoyl Chloride

entry	catalyst	mass (mg)	time (h)	run	conversion[a] (%)
1	none		10	1	<5
2	Si(HIPE)	28.1	10	1	32
3	Nb_2O_5	31.0	10	1	41
4	MUB-105(3)	23.4	10	1	100 (95)[b]
5−8	MUB-105(3)	23.4	10	2−8	100
9	MUB-105(3)	22.9	10	9	80
10	MUB-105(2)	23.4	10	1	100 (93)[b]
11−19	MUB-105(2)	27.6	10	2−8	100
20	MUB-105(2)	27.6	10	9	77
21	MUB-105(1)	31.1	10	1	100 (92)[b]
22−28	MUB-105(1)	23.7	10	2−8	100
29	MUB-105(1)	23.7	10	9	95

[a]The solution was analyzed during the reactions by HPLC. Anisole (50 mmol), benzoyl chloride (1 mmol), T = 140 °C. [b]Isolated yields of pure products obtained through chromatography column. Only the para-acylated product is obtained (Figure S7).

Nb_2O_5 or Si-(HIPE) (entries 2, 3) yield conversions of 41 and 32%, respectively. Beyond the conversion percentage, we emphasize the extremely high selectivity (Figure S4). Although statistically we should obtain 2/3 of the ortho product and 1/3 of the para product, this is not the case, as we obtained ∼93% of the para-substituted product (Table 6, entries 4, 10, 21).

As for the alkylation, the catalysts can be cycled, yielding 100% conversion (Table 6, entries 2, 5−8, 10, 11−19, 21, 22−28) for the first eight cycles, after which the conversion yield starts to decrease (entries 20, 29).

Both of the catalyzed reactions involve Nb_2O_5 particles present at the macropore surface (this is the case even for MUB-105(1) bearing the smallest nanoparticles), such that the active sites are not confined within the mesoporosity. In terms of fluid hydrodynamics, the fluid behavior within the macropore is hybrid, implicating a convective Poiseuille[41] flow at the macropore center, whereas in the vicinity of the solid−liquid macropore border, the scenario is the one of a liquid bearing a low but non-negligible convection. The molecules diffuse within the convection, giving an interfacial dispersion behavior (also seen in mesopores), well-known as the "Taylor-Aris" dispersion.[42,43] This feature has been shown[44] to be a main characteristic of efficient heterogeneous catalysts. Moreover, another aspect favors high efficiency: all the active sites are found in the vicinity of the macropores and not trapped in the mesoporous structure, thereby offering high accessibility and low molecular hindrance. The combination of these two parameters is certainly of major importance in explaining the observed efficiency (Tables 4−6). Besides the fluid hydrodynamics within the macropores being constant in all the materials (dispersive behavior in the vicinity of the macropores), the intimate structure and dispersity of the Nb_2O_5 crystals can explain the increasing efficiency of the catalysts as the Nb_2O_5 content decreases from MUB-105(3) to MUB-105(1). This latter catalyst bears the smallest Nb_2O_5 particles sizes and lowest Nb_2O_5 content (and thus the highest dispersity and active surface area) but additionally, the highest amorphous character as revealed by XRD and Raman spectroscopy. This feature that is known to favor the Brønsted acid sites in the distorted polyhedra of amorphous $Nb_2O_5 \cdot nH_2O$.[29] In the present case, the surface acidic concentration drastically increases from 12, 73, and 410 μmol g^{-1}, respectively, from MUB-105(3) to the MUB-105(2) and MUB-105(1) as expressed with NH_3-TPD. Overall the MUB-105(1) catalyst offers high Nb_2O_5 dispersity, low particle size, high active surface area, the lowest crystalline character, and structural, textural, and morphological characteristics that intrinsically improve its catalytic properties.

Finally, we have investigated the spent catalysts to estimate the reason for the decreasing efficiency when cycling. First, at the macroscopic scale, we notice that the macroscopic cells remain unchanged, where Nb_2O_5 crystals can be evidenced especially for the spent MUB-105(2) and MUB-105(3) catalysts (Figure S8). TEM investigations at the mesoscopic scale demonstrate that the evolution of particle sizes and aggregation is rather low (Figures S9 and S10). We do not, for example, observe obvious evidence of particle aggregation or particle leaching resulting in a diminished size. As a direct consequence, WAXS experiments of the spent catalysts (Figure S11a, b) resemble those prior to performing the catalytic tests, and an increase in the amorphous character of the nanocrystals is not observed. To get further insight into the surface composition and chemical states of the materials after catalysis, we performed X-ray photoelectron spectroscopy investigations (XPS) after 7 catalytic runs (Figures S12−S17). After the catalytic cycles, similar features were found for the Nb 3d and Si 2p regions, indicating that the catalytic process did not induce significant changes in the oxidation state of niobium. The main differences concern the carbon amount, which is much higher for the catalysts after the alkylation reactions (Table S2). Moreover, fitting of the C 1s region yields four contributions at 284.4 ± 0.1, 285.0 ± 0.1, 286.3 ± 0.1, and 287.3 ± 0.1 eV, which can be assigned to C_{sp2}-C_{sp2}, C_{sp3}-C_{sp3}, C−O, and C═O species, respectively.[45] Thus, for MUB-105(3), the presence of C−O species after acylation reactions suggests the pollution of the catalysts by reaction products, and this organic poisoning of the catalysts after several runs could explain the decrease in catalytic activity while cycling.

4. CONCLUSIONS

We have designed the first series of Nb_2O_5−SiO_2(HIPE) self-standing monolithic catalysts bearing multiscale porosity through the integration of sol−gel processing and the physical chemistry of complex fluids.[46] These porous materials offer an average porosity of 96%, providing surface areas between 700 and 1100 m^2 g^{-1}. The specific surface area increases as the nanoparticle size decreases from the MUB-105(3) to the MUB-105(1) catalysts, revealing that the nanoparticles provide additional surface area and thus cannot be embedded within the mesoscopic channels, but rather are dispersed at the surface of the macropores, as further supported by SAXS investigations. This feature appears to be very important in allowing the substrate to easily access the catalytic sites. At the microscopic scale, both WAXS and Raman investigations reveal the less crystalline pseudohexagonal TT-Nb_2O_5

allotropic form, where nanocrystals contain distorted NbO_6 octahedra, NbO_7 pentagonal bipyramids, and NbO_8 hexagonal bipyramids. NH_3-TPD reveals that although the acidic site concentration is drastically increased from MUB-105(3) to MUB-105(1), the acidic strength slightly decreases. The MUB-105 series has been tested toward liquid-phase and solvent-free heterogeneous catalysis of Friedel–Crafts alkylation and acylation reactions, where 100% conversion has been reached at 140 °C while cycling. Considering the alkylation reaction, MUB-105(1) yields the highest TON of 836 and TOF of 9 h^{-1}, whereas for the acylation, MUB-105(1) and MUB-105(2) yield the highest TON of 1010 and TOF of 13 h^{-1}. Moreover, we found out that the catalysts are selective in producing 50/50% of ortho- and para-substituted monoalkylated products, whereas in the acylation reaction, the selectivity is higher, with around 90% yield of the para-substituted acylated product. XPS studies revealed some organic poisoning of the catalysts after several runs, which could explain the decrease in catalytic activity during cycling. The catalysts presented here are in a monolithic self-standing state and not powder, thereby offering handling ease for reuse and extraction from the final products.

■ ASSOCIATED CONTENT

Supporting Information

The Supporting Information is available free of charge at https://pubs.acs.org/doi/10.1021/acsami.1c24554.

TGA experiments, Porod-like representation of the small-angle scattered intensities, complementary SEM, TEM, WAXS, NH_3-TPD, and XPS data of the spent catalysts (PDF)

■ AUTHOR INFORMATION

Corresponding Authors

Rénal Backov − *CRPP-UMR CNRS 5031, Université de Bordeaux, Pessac 33600, France;* orcid.org/0000-0001-5946-8917; Email: renal.backov@crpp.cnrs.fr

Frédéric Louërat − *CRPP-UMR CNRS 5031, Université de Bordeaux, Pessac 33600, France*; Email: frederic.louerat@crpp.cnrs.fr

Authors

Isabelle Ly − *CRPP-UMR CNRS 5031, Université de Bordeaux, Pessac 33600, France*

Elodie Layan − *CRPP-UMR CNRS 5031, Université de Bordeaux, Pessac 33600, France*

Emmanuel Picheau − *CRPP-UMR CNRS 5031, Université de Bordeaux, Pessac 33600, France;* orcid.org/0000-0002-6921-4555

Nicolas Chanut − *Department of Civil and Environmental Engineering, Massachusetts Institute of Technology, MIT Energy Initiative, Cambridge, Massachusetts 02139, United States*

Frédéric Nallet − *CRPP-UMR CNRS 5031, Université de Bordeaux, Pessac 33600, France*

Ahmed Bentaleb − *CRPP-UMR CNRS 5031, Université de Bordeaux, Pessac 33600, France*

Marie-Anne Dourges − *CNRS, Bordeaux INP, ISM, UMR 5255, Université de Bordeaux, Talence Cedex F-33405, France*

Roland J. Pellenq − *Department of Civil and Environmental Engineering, Massachusetts Institute of Technology, MIT Energy Initiative, Cambridge, Massachusetts 02139, United States*

Elizabeth A. Hillard − *ICMCB-UMR CNRS 5026, Université de Bordeaux, Pessac Cedex 33608, France;* orcid.org/0000-0002-5149-0324

Thierry Toupance − *CNRS, Bordeaux INP, ISM, UMR 5255, Université de Bordeaux, Talence Cedex F-33405, France;* orcid.org/0000-0001-8234-7064

François Dole − *CRPP-UMR CNRS 5031, Université de Bordeaux, Pessac 33600, France*

Author Contributions

The manuscript was written through contributions of all authors.

Funding

This study received financial support from the French government in the framework of the University of Bordeaux's IdEx "Investments for the Future" program/GPR PPM.

Notes

The authors declare no competing financial interest.

■ ACKNOWLEDGMENTS

R.B. thanks Sabrina Lacomme (Bordeaux Imaging Center-BIC) for the TEM investigations, Christine Labrugère for the XPS acquisition (PLACAMAT)-Bordeaux. The authors thank the PhD student Charlotte Croisé (IC2MP-Poitiers) for acquiring the NH_3-TPD data set. This work benefited from the facilities and expertise of the CESAMO platform (Bordeaux University).

■ REFERENCES

(1) Silverstein, M. S. Recent Advances in Emulsion-templated Porous Polymers. *Prog. Polym. Sci.* **2014**, *39*, 199–234.

(2) Silverstein, M. S. Emulsion-templated polymers: Contemporary Contemplations. *Polymer* **2017**, *126*, 261–282.

(3) Silverstein, M. S. The Chemistry of Porous Polymers: The Holy Grail. *Israel. J. Chem.* **2020**, *60*, 140–150.

(4) Araya, A. Hydrophobic, Highly Porous, Three-Dimensional Inorganic Structures. U.S. Patent 4 888 309, 1989.

(5) Carn, F.; Colin, A.; Achard, M.-F.; Deleuze, H.; Sellier, E.; Birot, M.; Backov, R. Inorganic Monoliths Hierarchically Textured via Concentrated Direct Emulsion and Micellar Templates. *J. Mater. Chem.* **2004**, *14*, 1370–1376.

(6) Brun, N.; Ungureanu, S.; Deleuze, H.; Backov, R. Hybrid Foams, Colloids and Beyond: From Design to Applications. *Chem. Soc. Rev.* **2011**, *40*, 771–788.

(7) Roucher, A.; Depardieu, M.; Pekin, D.; Morvan, M.; Backov, R. Inorganic, Hybridized and Living Macrocellular Foams: "Out of the Box" Heterogeneous Catalysis. *Chem. Record.* **2018**, *18*, 776–787.

(8) Roucher, A.; Morvan, M.; Pekin, D.; Depardieu, M.; Blin, J.-L.; Schmitt, V.; Konrad, M.; Baret, J.-C.; Backov, R. From Compartmentalization of Bacteria within Inorganic Macrocellular Beads to the Assembly of Microbial Consortia. *Adv. Biosystems* **2018**, *2*, 1700233.

(9) Brun, N.; Babeau-Garcia, A.; Achard, M.-F.; Sanchez, C.; Durand, F.; Laurent, G.; Birot, M.; Deleuze, H.; Backov, R. Enzyme-Based Biohybrid Foams Designed for Continuous Flow Heterogeneous Catalysis and Biodiesel Production. *Energy Environ. Sci.* **2011**, *4*, 2840–2844.

(10) Gaikwad, P.; Ungureanu, S.; Backov, R.; Vynck, K.; Vallée, R. A. L. Photon Transport in Cylindrically-Shaped Disordered Meso-macroporous Materials. *Optic Express* **2014**, *22*, 7503–7513.

(11) Bachelard, N.; Gaikwad, P.; Backov, R.; Sebbah, P.; Vallée, R. A. L. Disorder as a Playground for the Coexistence of Optical

Nonlinear Effects: Competition between Random Lasing and Stimulated Raman Scattering in Complex Porous Materials. *ACS Photonics* **2014**, *1*, 1206−1211.
(12) Gaikwad, P.; Bachelard, N.; Sebbah, P.; Backov, R.; Vallee, R. A. L. Competition and Coexistence of Raman and Random Lasing in Silica-Titania-Based Solid Foams. *Adv. Optical Mater.* **2015**, *3*, 1640−1651.
(13) Bernadet, S.; Tavernier, E.; Ta, D.-M.; Vallée, R. A. L.; Ravaine, S.; Fécant, A.; Backov, R. Bulk Photo-Driven CO_2 Conversion through TiO_2@Si(HIPE) Monolithic Macrocellular Foams. *Adv. Funct Mater.* **2019**, *29*, 1807767.
(14) Debecker, D. P.; Boissiere, C.; Laurent, G.; Huet, S.; Eliaers, P.; Sanchez, C.; Backov, R. First Acidic Macro-Mesocellular Aluminosilicate Monolithic Foams "SiAl(HIPE)" and their Catalytic Properties. *Chem. Commun.* **2015**, *51*, 14018−14021.
(15) Roucher, A.; Bentaleb, A.; Laurichesse, E.; Dourges, M.-A.; Emo, M.; Schmitt, V.; Blin, J.-L.; Backov, R. First Macro-Mesocellular Silica SBA-15-Si(HIPE) Monoliths: Conditions for Obtaining Self-Standing Materials. *Chem. Mater.* **2018**, *30*, 864−873.
(16) Roucher, A.; Emo, M.; Vibert, F.; Stébé, M.-J.; Schmitt, V.; Jonas, F.; Backov, R.; Blin, J.-L. Investigation of Mixed Ionic/Nonionic Building Blocks for the Dual Templating of Macro-Mesoporous Silica Foams. *J. Colloid Interface Sci.* **2019**, *533*, 385−400.
(17) Llordés, A.; Garcia, G.; Gazquez, J.; Milliron, D. J. Tunable Near-Infrared and Visible-Light Transmittance in Nanocrystal-in-Glass Composites. *Nature.* **2013**, *500*, 323−326.
(18) Wu, J.; Li, J.; Lü, X.; Zhang, L.; Yao, J.; Zhang, F.; Huang, F.; Xu, F. A One-Pot Method to Grow Pyrochlore $H_4Nb_2O_7$-Octahedron-based Photocatalyst. *J. Mater. Chem.* **2010**, *20*, 1942−1946.
(19) Nakajima, K.; Baba, Y.; Noma, R.; Kitano, M.; Kondo, J. N.; Hayashi, S.; Hara, M. $Nb_2O_5{\cdot}nH_2O$ as a Heterogeneous Catalyst with Water-Tolerant Lewis acid sites. *J. Am. Chem. Soc.* **2011**, *133*, 4224−4227.
(20) Murayama, T.; Chen, J.; Hirata, J.; Matsumoto, K.; Ueda, W. Hydrothermal Synthesis of Octahedra-based Layered Niobium Oxide and Its Catalytic Activity as a Solid Acid. *Catal. Sci. Technol.* **2014**, *4*, 4250−4257.
(21) Brunauer, S.; Emmett, P. H.; Teller, E. Adsorption of Gases in Multimolecular Layers. *J. Am. Chem. Soc.* **1938**, *60*, 309−319.
(22) Brinker, C. J.; Scherer, G. W. Sol−Gel Science. In *The Physics and Chemistry of Sol−Gel Processing*; Academic Press, 1990; pp 1−912.
(23) Porod, G. In *Small Angle X-ray Scattering*; Glatter, O., Kratky, O. Academic Press: London, 1982; Chapter 2, pp 17−51.
(24) Jehng, J. M.; Wachs, I. E. Structural Chemistry and Raman Spectra of NiobiumOxides. *Chem. Mater.* **1991**, *3*, 100−107.
(25) Brayner, R.; Bozon-Verduraz, F. Niobium Pentoxide Prepared by Soft Chemical Routes: Morphology, Structure, Defects and Quantum Size Effect. *Phys. Chem. Chem. Phys.* **2003**, *5*, 1457−1466.
(26) Denofre, S.; Gushikem, Y.; de Castro, S. C.; Kawano, Y. ; Stability and Surface Acidity of Niobium(V) Oxide Grafted on a Silica Gel Surface. *J. Chem. Soc., Faraday Trans.* **1993**, *89*, 1057−1061.
(27) Morselli, S.; Moggi, P.; Cauzzi, D.; Predieri, G. Preparation and Characterization of Niobia and Silica-Niobia systems. *Stud. Surf. Sci. Catal.* **1998**, *118*, 763−772.
(28) Burke, P. A.; Weissman, J. G.; Ko, E. I.; Wynblatt, P. In *Catalysis*; Wards, J. W., Ed.; Elsevier: Amsterdam, 1987; p 457.
(29) Lebarbier, V.; Houalla, M.; Onfroy, T. New Insights into the Development of Brønsted Acidity of Niobic Acid. *Catal. Today.* **2012**, *192*, 123−129.
(30) Tanabe, K.; Hölderich, W. F. Industrial Application of Solid Acid−Base Catalysts. *Appl. Catal., A* **1999**, *181*, 399−434.
(31) Degioanni, S.; Jurdyc, A. M.; Cheap, A.; Champagnon, B.; Bessueille, F.; Coulm, J.; Bois, L.; Vouagner, D. Surface-Enhanced Raman Scattering of Amorphous Silica Gel Adsorbed on Gold Substrates for Optical Fiber Sensors. *J. Appl. Phys.* **2015**, *118*, 153103.
(32) Trung Tran, S. B.; Choi, H.; Oh, S.; Park, J. Y. Influence of Support Acidity of Pt/Nb_2O_5 Catalysts on Selectivity of CO_2 Hydrogenation. *Catal. Lett.* **2019**, *149*, 2823−2835.
(33) Han, X.; Russo, P. A.; Goubard-Bretesché, N.; Patané, S.; Santangelo, S.; Zhang, R.; Pinna, N. Exploiting the Condensation Reactions of Acetophenone to Engineer Carbon-Encapsulated Nb_2O_5 Nanocrystals for High-Performance Li and Na Energy Storage Systems. *Adv. Ener. Mater.* **2019**, *9*, 1902813.
(34) Mokhtar, S. M.; Ahmad, M. K.; Harish, S.; Hamed, N. K. A.; Shimomura, M. Surface Chemistry and Growth Mechanism of Highly Oriented, Single Crystalline Nb-doped TiO_2 Nanorods. *CrystEngCommun.* **2020**, *22*, 2380−2388.
(35) King, B. R.; Patel, H. C.; Gulino, D. A.; Tatarchuk, B. J. Kinetic Measurements of Oxygen Disssolution into Niobium Substrates: In Situ X-ray Photoelectron Spectrosocpy Studies. *Thin Solid Films* **1990**, *192*, 351−369.
(36) Suja, H.; Deepa, C. S.; Sreejarani, K.; Sugunan, S. Acidity and Catalytic Activity of Sulphate Modified Mixed Oxides of Tin and Praseodymium. *React. Kinet. Catal.* **2000**, *71*, 307−311.
(37) Pereira, C. C. M.; Lachter, E. R. Alkylation of Toluene and Anisole with 1-octen-3-ol over Niobium catalysts. *Appl. Catal., A* **2004**, *266*, 67−72.
(38) Takagaki, A.; Lu, D.; Kondo, J. N.; Hara, M.; Hayashi, S.; Domen, K. Exfoliated HNb_3O_8 Nanosheets as a Strong Protonic Solid Acid. *Chem. Mater.* **2005**, *17*, 2487−2489.
(39) Murayama, T.; Chen, J.; Hirata, J.; Matsumoto, K.; Ueda, W. Hydrothermal Synthesis of Octahedra-based Layered Niobium Oxide and its Catalytic Activity as a Solid Acid. *Catal. Sci. Technol.* **2014**, *4*, 4250−4257.
(40) de la Cruz, M. H.C.; Abdel-Rehim, M. A.; Rocha, A. S.; da Silva, J. F.C.; da Costa Faro, A.; Lachter, E. R. Liquid Phase Alkylation of Anisole by Benzyl Alcohol Catalyzedon Alumina-Supported Niobia. *Catal. Commun.* **2007**, *8*, 1650−1654.
(41) Guyon, E.; Hulin, J. P.; Petit, C.; Mitescu, C. D. In *Physical Hydrodynamics*; Oxford University Press, 2001.
(42) Aris, R. On the Dispersion of a Solute in a Fluid Flowing through a Tube. *Proc. R. Soc. A* **1956**, *235*, 67−77.
(43) Taylor, G. I. Dispersion of Soluble Matter in Solvent Flowing Slowly through a Tube. *Proc. R. Soc. A* **1953**, *219*, 186−203.
(44) Ungureanu, S.; Deleuze, H.; Popa, M. I.; Sanchez, C.; Backov, R. First Pd@organo-Si(HIPE) Open-Cell Hybrid Monoliths Generation Offering Cycling Heck Catalysis Reactions. *Chem. Mater.* **2008**, *20*, 6494−6500.
(45) Han, X.; Russo, P. A.; Triolo, C.; Santangelo, S.; Goubard-Bretesché, N.; Pinna, N. Comparing the Performance of Nb_2O_5 Composites with Reduced Graphene Oxide and Amorphous Carbon in Li- and Na-ion Electrochemical Storage Devices. *ChemElectroChem.* **2020**, *7*, 1689−1698.
(46) Backov, R. Combining Soft Matter and Soft Chemistry: Integrative Chemistry towards Designing Novel and Complex Multiscale Architectures. *Soft Matter* **2006**, *2*, 452−464.